

Dry Electrode Processing for High-Performance Molten Salt Batteries

Kuangyu Wang, Yulong Wu, Cheng Yang, Maosheng Yu, Chong Lei, Yingchuan Zhang, Tiezheng Ding, Yuanzheng Long, Kai Liu,* Meicheng Li, and Hui Wu

Molten salt batteries (MSBs) are renowned for their rapid reaction kinetics, high safety, and cost-effectiveness. However, their electrode design faces challenges due to polymer binder incompatibility in molten salt electrolytes (MSEs). To address this, an expanded graphite (EG) electrode is proposed through a dry electrode processing method for MSE-based aluminum-ion batteries. This method facilitates the fabrication of large-area electrodes featuring high active material loadings of up to $\approx 60 \text{ mg cm}^{-2}$. Notably, the EG electrode exhibits remarkable rate performance, achieving a specific capacity of 84.4 mAh g^{-1} in the $\text{AlCl}_3\text{-NaCl-KCl}$ MSE at $125 \text{ }^\circ\text{C}$ with a current density of 5 A g^{-1} . This outstanding performance can be attributed to its rapid multi-step intercalation reaction kinetics and well-developed pore structure. Leveraging the chemical stability and fibrillation binding mechanism of the polytetrafluoroethylene binder, the electrode demonstrates longevity over 10,000 cycles, despite experiencing a three-fold volume expansion. Additionally, a 100-mAh-scale Al-EG full-cell cycled 100 times with an energy efficiency of 78.7% at 500 mA underscores its potential for large-scale applications. Considering the broad applicability of this approach, it can also provide crucial references and insights for electrode design across various MSB systems.

electrolytes.^[4,5] In response, molten salt batteries (MSBs), characterized by their utilization of molten salt electrolytes (MSEs), have shown promising application prospects owing to their fast reaction kinetics, intrinsic safety features, and cost-effectiveness.^[6–8] Notably, various MSB systems have been explored by researchers, encompassing thermally activated batteries,^[9] liquid metal batteries,^[10] metal-air batteries,^[11–13] and aluminum-ion batteries,^[14] all exhibiting commendable electrochemical performance.

However, compared to ambient-temperature battery systems, MSBs encounter significant limitations in the design of electrode compositions and structures. Currently, electrode materials employed in MSE environments can be broadly classified into three categories. The first category comprises self-supporting metal or carbon-based materials, exemplified by aluminum foils and graphite papers used in aluminum-ion batteries^[15–17] and metal electrodes

used in metal-air batteries.^[11,18] The second category consists of molten metals or alloys used in the liquid metal batteries.^[19,20] Lastly, densely compacted powdery active materials are employed in thermally activated batteries.^[21–23] However, it is evident that the first two electrode structures are only applicable to very limited materials and lack electrolyte infiltration, while the third type of electrode faces challenges such as structural looseness, inadequate stability, and suboptimal conductivity, all of which impose constraints on the design of battery configurations.

Therefore, it becomes imperative to develop an electrode preparation method that accommodates various active materials while ensuring stable operation within the MSE environment. As we scrutinize the most prevalent lithium-ion battery electrodes, it is evident that binders constitute one of the key components. They serve the purpose of adhering to the powders to the current collector and ensuring cohesion among the powders throughout the bulk of the electrode.^[24] Nevertheless, the high-temperature environment and high reactivity of MSEs can potentially lead to the decomposition of most of the polymer binders, making electrode fabrication for MSBs an enduring challenge.^[25]


In recent years, the dry electrode processing method has witnessed widespread adoption in the fabrication of electrodes for

1. Introduction

The development of electrochemical energy storage technologies is of great significance for the utilization of renewable energy sources.^[1–3] Although lithium-ion batteries are currently the dominant electrochemical energy storage devices, they still pose safety risks due to the intrinsic properties of their

K. Wang, K. Liu, M. Li
State Key Laboratory of Alternate Electrical Power System with
Renewable Energy Sources
School of New Energy
North China Electric Power University
Beijing 102206, P. R. China
E-mail: liukai21@ncepu.edu.cn

K. Wang, Y. Wu, C. Yang, M. Yu, C. Lei, Y. Zhang, T. Ding, Y. Long, H. Wu
State Key Lab of New Ceramics and Fine Processing
School of Materials Science and Engineering
Tsinghua University
Beijing 100084, P. R. China

 The ORCID identification number(s) for the author(s) of this article can be found under <https://doi.org/10.1002/aenm.202400589>

DOI: 10.1002/aenm.202400589

electrochemical capacitors and lithium-ion batteries.^[26–28] Polytetrafluoroethylene (PTFE), renowned for its exceptional chemical stability and high resistance to corrosion, serves as a representative binder in this technique.^[29–31] The PTFE powders undergo plastic deformation in the electrode rolling step, forming a fibrous network during the preparation process, thus leading to the creation of a free-standing electrode.^[32–34] Importantly, this method balances both the mechanical strength and electrochemical kinetics of the electrode. Consequently, a higher active material loading can be achieved to meet the demanding requirements of high-energy-density applications.^[32]

Herein, we report an expanded graphite (EG) electrode for aluminum-ion batteries (AIBs) prepared via the dry electrode processing method. Electrodes with ultrahigh active material loadings up to $\approx 60 \text{ mg cm}^{-2}$ were obtained. In the $\text{AlCl}_3\text{-NaCl-KCl}$ molten salt electrolyte (ANK-MSE), the EG electrode delivered a specific capacity of 84.4 mAh g^{-1} at $125 \text{ }^\circ\text{C}$ with a current density of 5 A g^{-1} , attributed to its rapid multi-step intercalation reaction kinetics and well-structured pore structure. Leveraging the high stability and fibrillation binding mechanism of PTFE, the electrode maintained stability throughout over 10000 cycles. Over a broad temperature range of 100 to $175 \text{ }^\circ\text{C}$, the electrode consistently demonstrated superior overall electrochemical performance. Furthermore, a 100-mAh -scale Al-EG full-cell was assembled and operated for 100 cycles with an energy efficiency of 78.7% at 500 mA , demonstrating its potential for large-scale applications.

2. Results

2.1. Dry Electrode Processing of the EG Electrode

EG was selected as the cathode active material to accommodate the substantial volume expansion during the intercalation reactions due to its unique microstructures. According to the scanning electron microscopy (SEM) images, the EG powder predominantly consisted of layered particles (Figure S1, Supporting Information). The Brunauer-Emmett-Teller (BET) analysis revealed a large specific surface area of $18.9 \text{ m}^2 \text{ g}^{-1}$, with pore sizes predominantly ranging from 5 to 100 nm , contrasting regular graphite powders ($1.6\text{--}4.0 \text{ m}^2 \text{ g}^{-1}$), (Figure S2, Supporting Information). Transmission electron microscopy (TEM) images (Figure S3, Supporting Information) and X-ray diffraction (XRD) pattern (Figure S4, Supporting Information) indicated that the interlayer spacing remained unaltered compared to regular graphite.

Figure 1a illustrates a schematic diagram of the fabrication process of the EG electrode. During the calendaring process, PTFE formed fibrous network structures, serving as a binder for the active material and the carbon black (CB) conductive additive. This method enabled the production of a large-area free-standing electrode (Figure 1b), with adjustable electrode thicknesses within the range of $\approx 220\text{--}810 \text{ }\mu\text{m}$ (corresponding to active material loadings of $\approx 15\text{--}60 \text{ mg cm}^{-2}$) by varying the calendaring force (Figure 1c).

X-ray microcomputed tomography (micro-CT) was applied to gain comprehensive morphological information of the EG electrode. Figure 1d demonstrates the 3D reconstruction image of an EG electrode with a thickness of $\approx 220 \text{ }\mu\text{m}$, while horizontal and

vertical cross sectional slices are shown in Figure 1e,f, respectively. The prepared EG electrode possessed a porous structure, ensuring rapid electrolyte infiltration and ion transportation. Furthermore, it was observed that most of the pores in the vertical cross section slices appeared elongated in shape, indicating the alignment of the EG particles parallel to the calendaring direction.

2.2. Reaction Mechanisms of the EG Electrode

To clarify the electrochemical mechanisms of the EG electrode, we assembled a half-cell, using an aluminum foil as the reference electrode, a tantalum wire as the counter electrode, and the ANK-MSE as the electrolyte. Mo meshes with high electrochemical stability were used as the current collector for the EG electrode (Figure S5, Supporting Information). This electrolyte system employed inexpensive inorganic salts with a low eutectic point of $89.8 \text{ }^\circ\text{C}$ (Figure S6 and Table S1, Supporting Information). Its Raman spectrum exhibited two peaks at 370.9 and 307.6 cm^{-1} , corresponding to the AlCl_4^- and Al_2Cl_7^- ions, respectively, which are the predominant anions in this electrolyte system^[7,35] (Figure S7, Supporting Information). Figure S8 (Supporting Information) displays the electrochemical stability window of the ANK-MSE at $125 \text{ }^\circ\text{C}$. Aluminum deposition occurred when the potential was below 0 V , while chlorine gas evolved at potentials exceeding 2.20 V . Within the range of $1.00\text{--}2.05 \text{ V}$, the ANK-MSE could stably operate without decomposition.

During the charge process, multiple potential plateaus were observed in the range of $1.40\text{--}1.80 \text{ V}$, and a long potential plateau appeared at $\approx 1.85 \text{ V}$ in the galvanostatic charge/discharge (GCD) curve of the EG electrode ($\approx 220 \text{ }\mu\text{m}$ thickness) (Figure 2a). Correspondingly, a primary discharge plateau at $\approx 1.70 \text{ V}$ and a series of short plateaus in the range of 1.60 to 1.20 V were observed, indicating reversible multi-step electrochemical reactions.

Cyclic voltammetry (CV) tests were applied to investigate the kinetics of each electrochemical reaction. In theory, the voltammetric behavior of an electrode with different scan rates can be encapsulated as follows:^[36]

$$i = av^b \quad (1)$$

where i is the measured current, v is the sweep rate, and b reflects the charge storage mechanisms. In the case of a redox reaction primarily constrained by semi-infinite diffusion, b equals 0.5 . Conversely, for the capacitive behavior, b equals 1.0 . The CV curves of the EG electrode were tested with scan rates ranging from 1 to 10 mV s^{-1} (Figure 2b). Each CV curve exhibited three pairs of minor peaks (labeled as O1/R1, O2/R2, and O3/R3) and one pair of major peaks (labeled as O4/R4), with their corresponding positions consistent with those of the potential plateaus observed in the GCD curves. Through fitting, it was determined that the b values of the oxidation peaks were 0.87 , 0.85 , 0.93 , and 0.64 , while for the reduction peaks, they were 0.98 , 0.99 , 0.82 , and 0.78 , respectively (Figure 2c). This indicated that the reaction corresponding to the major peaks was close to that of battery electrodes, while the reactions corresponding to the other peaks displayed capacitor-like characteristics.

To further elucidate the reaction mechanisms, we prepared five electrode samples at different charge/discharge stages

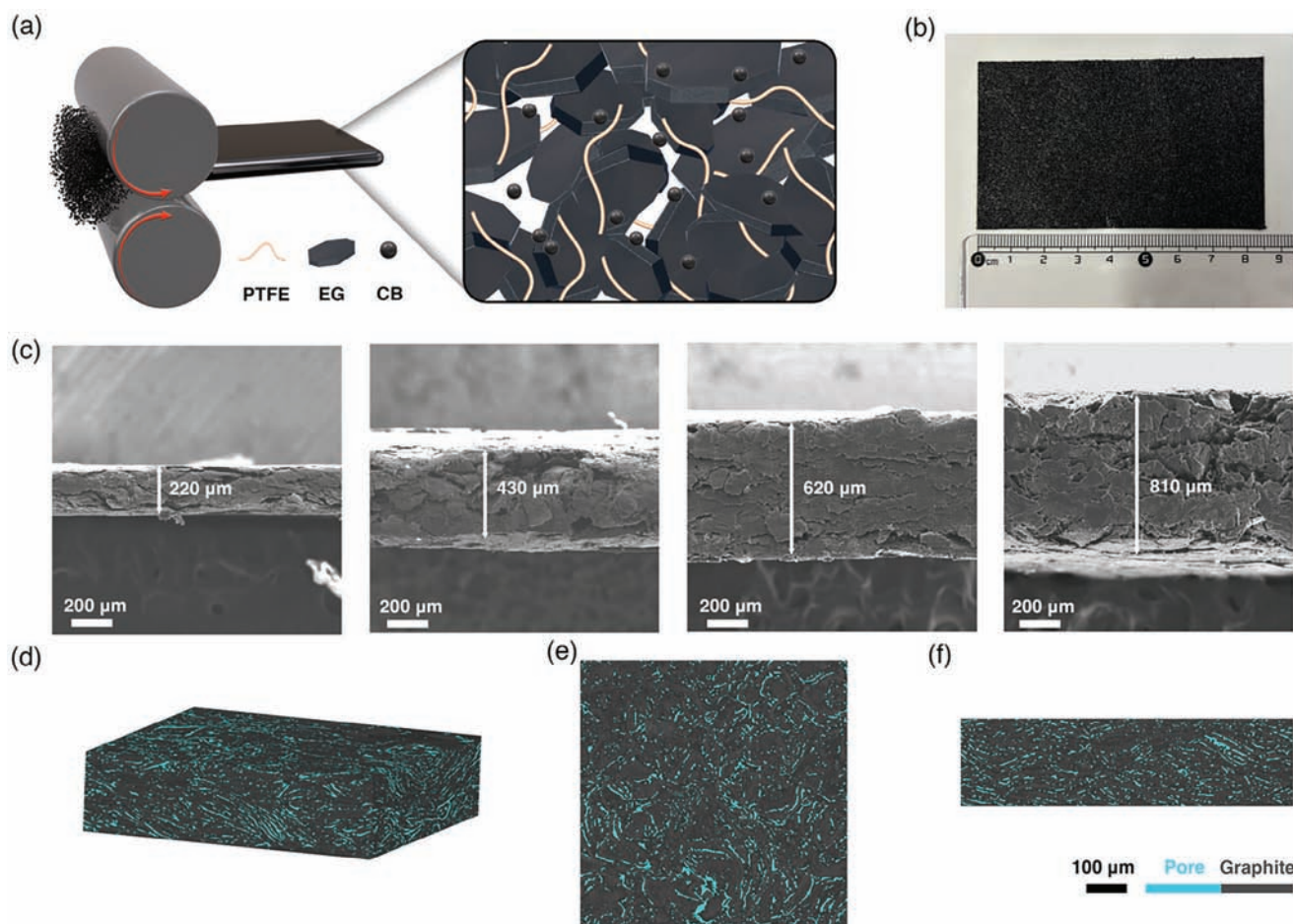


Figure 1. Dry electrode processing of the EG electrode. a) Schematic diagram of the fabrication process and microstructure of the EG electrode. b) Photograph of an EG electrode with a size of 8.5×5.0 cm. c) Sectional SEM images of the EG electrodes with different thicknesses. d) 3D reconstruction image of the EG electrode. e, f) Horizontal and vertical cross sectional slices of the 3D reconstruction image. Pores are represented in cyan, while EG particles are represented in gray-black.

(labeled as samples I–V) for ex situ XRD and Raman spectroscopy tests after ethanol cleaning to remove the electrolyte.

According to the XRD patterns, when the electrode was charged to 1.80 V (sample II), in addition to the (002) peak of graphite at 26.6° , a new peak at 27.2° was observed, indicating the possible formation of graphite intercalation compounds (GICs) through intercalation reactions (Figure S9, Supporting Information). Upon further charging to 2.05 V, sample III exhibited three peaks at 26.6° , 27.2° , and 27.5° , which might suggest the presence of GICs with different compositions in the electrode. It is noteworthy that sample IV showed similar peak positions to sample II, and the peak position of sample V was essentially the same as that in sample I, indicating good reversibility of the electrode reactions.

Analysis of Raman spectrums provided further insights. The graphite G band at 1582 cm^{-1} of both samples II and III split into a doublet of $E_{2g2}(i)$ mode and $E_{2g2}(b)$ mode, corresponding to the vibrations of carbon atoms in unperturbed graphene layers and bounding graphene layers adjacent to intercalated AlCl_4^- ions, respectively (Figure S10, Supporting Information).^[37,38] The peak positions of the $E_{2g2}(i)$ mode and $E_{2g2}(b)$ mode for sample

II were 1582 and 1603 cm^{-1} , respectively. For sample III, the values were 1585 and 1609 cm^{-1} , respectively, further confirming the generation of GICs with different compositions.

However, it is worth noting that the splitting of the G band was not observed in the Raman spectrums of samples IV and V. Additionally, compared to room-temperature systems, the peaks corresponding to the $E_{2g2}(b)$ mode in the spectrums of samples II and III were significantly weaker.^[39] As a result, we speculated that the highly reactive GICs might undergo decomposition or dissolution during ethanol cleaning. To address this issue, we conducted high-temperature XRD and Raman spectroscopy tests, where the electrolyte remained in the molten state. The liquid nature of the electrolyte resulted in the absence of XRD peaks, and its transparency characteristics facilitated the focusing of the laser beam used in the Raman spectroscopy tests. Specifically, we transferred the samples at different charge/discharge states to the XRD test system under the N_2 atmosphere for semi-in situ tests. Additionally, we conducted in situ Raman spectroscopy tests using the device shown in Figure 2d.

High-temperature XRD test results revealed significant changes in the spectrum of sample II, with the peak at 26.6° of

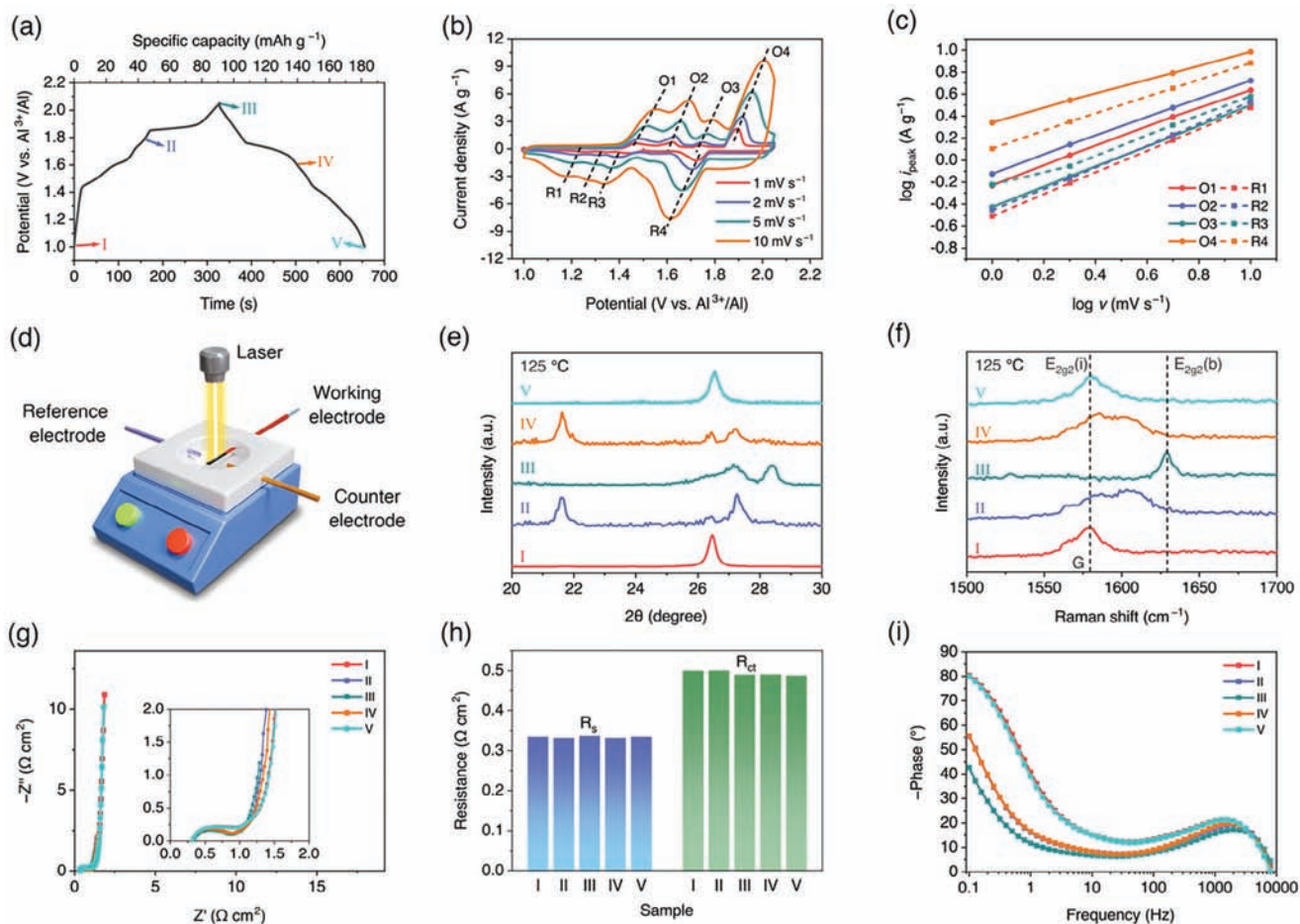
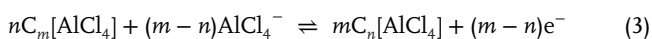


Figure 2. Reaction mechanisms of the EG electrode at 125 °C. a) Potential profile with a current density of 1 A g⁻¹. b) CV curves with different scan rates. c) Fitting results of the CV curves. d) Schematic diagram of the Raman spectroscopy test device. e) XRD patterns of samples I–V. f) Raman spectrums of the EG electrode at charge/discharge stages I–V. g–i) Nyquist plots, fitted results, and Bode plots of the EG electrode at charge/discharge stages I–V.

sample I replaced by two peaks at 21.6° and 27.2°, indicative of the staging phenomenon (Figure 2e).^[40] The main peaks of sample III were located at 27.1° and 28.4°, with a weak broad peak observed at ≈18.0° (Figure S11, Supporting Information). These results indicated the formation of GICs with lower stages during further charging.^[41] Additionally, the XRD peaks exhibited a tendency of left-shift compared to room-temperature systems, which might be attributed that the interlayer spacing between intercalated graphene layers was larger in the ANK-MSE system.

High-temperature Raman spectroscopy tests showed that the G band of the electrode at stage II split into the E_{2g2}(i) mode (1586 cm⁻¹) and E_{2g2}(b) mode (1603 cm⁻¹) (Figure 2f). Upon completion of the charge process, the peak corresponding to the E_{2g2}(i) mode nearly disappeared, while the peak corresponding to the E_{2g2}(b) mode continued to right-shift to 1629 cm⁻¹ at stage III, indicating the complete intercalation of the AlCl₄⁻ ions in the EG electrode. Consequently, the multi-step intercalation reactions of the EG electrode can be summarized as follows:



Based on the characterization results above, it was determined that the multiple oxidation-reduction peaks in the CV curves of the EG electrode corresponded to intercalation reactions at different stages. However, the precise origins of their reaction kinetic disparities remained ambiguous. Therefore, electrochemical impedance spectroscopy (EIS) measurements were conducted (Figure 2g). Figure S12 (Supporting Information) illustrates the equivalent circuits used for quantitative analysis, where R_s represents the solution resistance, and R_{ct} represents the charge transfer resistance. Notably, no significant discrepancies were observed in R_s and R_{ct} at charge/discharge stages I–V (Figure 2h). Since R_s is mainly associated with electrolyte resistance, it remained constant under the consistent testing temperature. R_{ct} reflects the electrochemical activity of the electrode, which also exhibited stability throughout the intercalation reactions. However, substantial variations were noted in the phase angles within the low-frequency region, indicative of different diffusion-limited behavior at different charge/discharge stages (Figure 2i).^[42] Specifically, at 0.1 Hz, the phase angles of the electrode at stages I–V were -80.3°, -55.3°, -42.7°, -55.7°, and -79.9°, respectively. These phase angles closely corresponded to their respective intercalation stages. It is worth noting that the

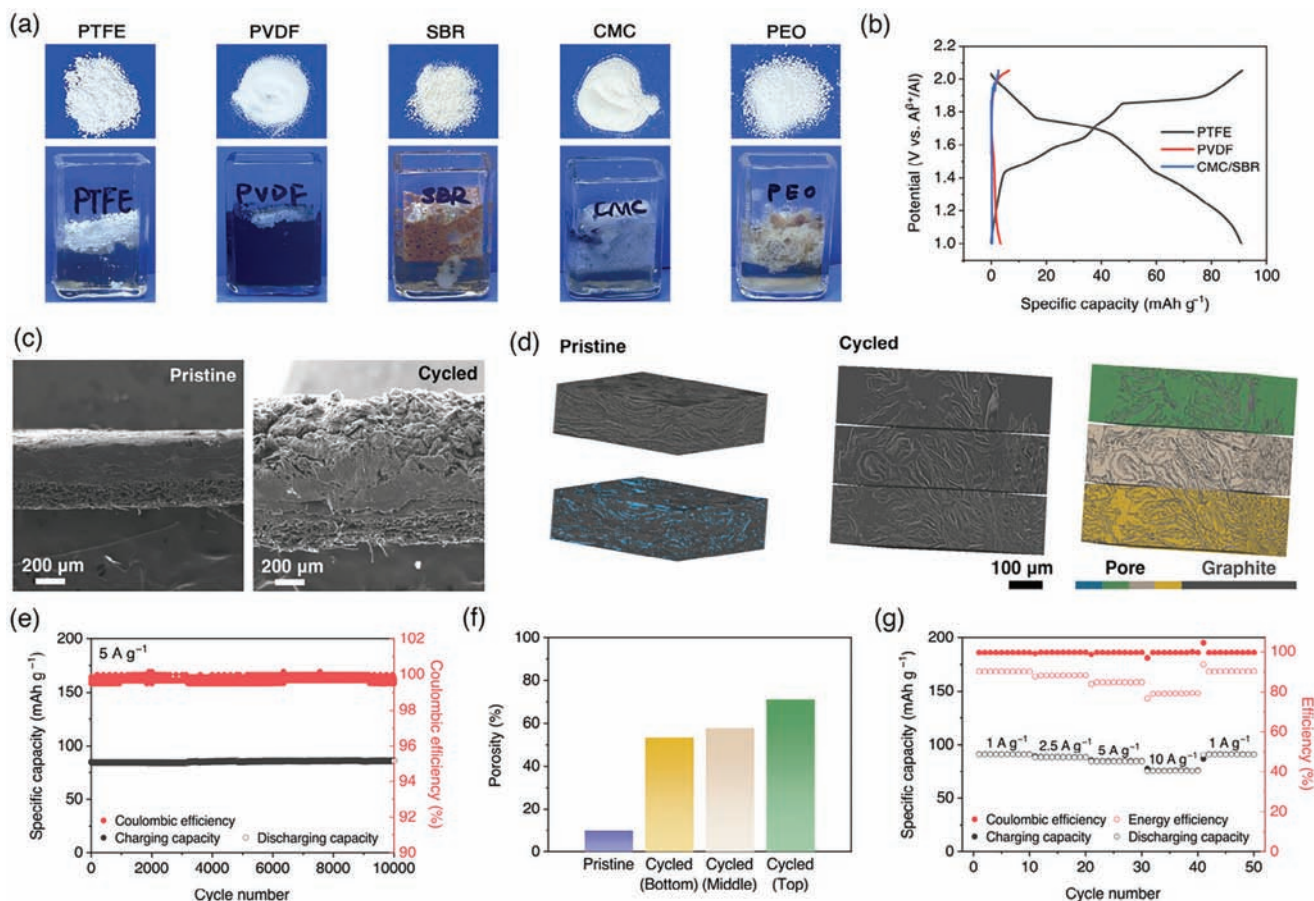


Figure 3. Working mechanisms of the PTFE binder. a) Chemical stability of different binders in the ANK-MSE. b) GCD curves of the EG electrodes using different binders with a current density of 1 A g^{-1} at $125 \text{ }^\circ\text{C}$. c) SEM images and 3D reconstruction images of the EG electrode at the pristine state and after the first cycle. The 3D reconstruction image of the EG electrode after the first cycle is divided into three sections for analysis. Pores are represented in blue, green, beige, and yellow, while EG particles are represented in gray-black. e) Cycling stability of the EG electrode at $125 \text{ }^\circ\text{C}$. f) Porosities of the EG electrode at the pristine state and after the first cycle. g) Rate performance of the EG electrode at $125 \text{ }^\circ\text{C}$.

phase angle of a pure resistor is 0° , while phase angles of -45° and -90° indicate a diffusion-limited response and a purely capacitive response, respectively.^[43] As a result, as the intercalation reactions progressed, the electrode's electrochemical response gradually decelerated due to diffusion control, leading to a deviation of the electrode properties from capacitive characteristics toward more battery-like behaviors.

In summary, through a combination of electrochemical tests and structural characterizations, we elucidated the multi-step intercalation reaction mechanisms of the EG electrode. During the initial phases of the intercalation reactions, the electrode exhibited rapid reaction kinetics with capacitive characteristics. A gradual decrease in the reaction kinetics was observed as intercalation proceeded, attributed to the increased diffusion limitations experienced by AlCl_4^- ions.

2.3. Working Mechanisms of the PTFE Binder

The chemical stability of the PTFE binder played a crucial role in achieving superior electrochemical performance of the electrode.

As depicted in **Figure 3a**, PTFE powder maintained its structural integrity in the ANK-MSE, while commonly used binders for wet electrode processing such as polyvinylidene difluoride (PVDF), styrene-butadiene rubber (SBR), carboxymethyl cellulose (CMC), and polyethylene oxide (PEO) exhibited color changes, volume expansion, and even gas generation. According to the GCD curve at $125 \text{ }^\circ\text{C}$, the EG electrode achieved a specific capacity of 90.9 mAh g^{-1} and an impressive half-cell energy efficiency of 90.2% with a current density of 1 A g^{-1} (**Figure 3b**). In contrast, EG electrodes prepared with alternative binders displayed negligible capacity in the ANK-MSE system.

To investigate the microstructure evolution of the EG electrode, Mo meshes were replaced with carbon papers as the current collectors to perform SEM (**Figure 3c**) and micro-CT characterizations (**Figure 3d**). The results indicated that the EG electrode experienced a nearly threefold expansion after the first cycle. Further research found that when the electrode was charged to 1.80 V in the first cycle, the expansion of the electrode was essentially completed (**Figure S13**, Supporting Information). During the discharge process, where deintercalation reactions occurred, the thickness of the electrode remained nearly

unchanged, indicating irreversible microstructure evolution. SEM images captured at higher magnification revealed that the PTFE binder was further stretched along the thickness under the influence of internal stresses caused by volume expansion (Figure S14, Supporting Information).

Despite experiencing significant volume expansion during the cycling process, the electrode still exhibited excellent cycling stability. With a current density of 5 A g⁻¹, the electrode maintained a discharging capacity of 85.8 mAh g⁻¹ even after 10000 cycles, with an average coulombic efficiency of 99.7% (Figure 3e). The GCD curves of the initial and final three cycles also revealed minimal alteration in the potentials of the charge/discharge plateaus (Figure S15, Supporting Information). Figure S16 (Supporting Information) illustrates the microstructures of the electrode before and after cycling. It was observed that even after 10000 cycles, the electrode particles remained in close contact under the influence of the PTFE binder, with no particle fragmentation or detachment observed.

In addition to accommodating volume expansion and maintaining structural stability, the use of the PTFE binder enabled the fabrication of porous electrodes. The presence of a rich pore structure within the electrode facilitated rapid ion transport, resulting in high rate performance of corresponding devices. According to the micro-CT images, the layered EG particles within the electrode underwent separation and tilting due to the influence of internal stresses after the reactions (Figure 3d). Naturally, the porosity of the electrode significantly increased. To quantitatively analyze the electrode's porosity, we divided the 3D reconstruction of the cycled electrode into three sections (bottom, middle, and top) along the thickness, and calculated the porosity of each section. As depicted in Figure 3f, the electrode's porosity increased from 10% before cycling to 53%, 58%, and 71% in the bottom, middle, and top layers, respectively, after cycling.

Consequently, the EG electrode exhibited excellent rate performance, with its discharging capacity with current densities of 1, 2.5, 5, and 10 A g⁻¹ reaching 90.9, 88.2, 84.4, and 75.8 mAh g⁻¹, respectively (Figure 3g). When the current density was readjusted to 1 A g⁻¹, the discharging capacity recovered to 90.8 mAh g⁻¹, demonstrating the electrode's excellent adaptability to real-world application environments.

It is noteworthy that, despite the volume expansion of the electrode leading to a certain degree of structural non-uniformity, there was no significant difference in the energy storage capacity of the electrode material along the thickness. The Raman spectrums of different regions of the electrode at stage III are shown in Figure S17 (Supporting Information), with their main peaks all located at 1630 cm⁻¹, corresponding to the E_{2g2}(b) mode of the intercalated EG.

Moreover, the structural characteristics of the porous electrode enable the facile customization of electrodes for diverse application scenarios by adjusting material compositions and preparation methods. For instance, to address the demands of high-power-density applications, thinner electrodes were prepared. As depicted in Figure S18a (Supporting Information), the EG electrode with a thickness of ≈80 μm achieved a specific capacity of 81.7 mAh g⁻¹ and a half-cell energy efficiency of 80.5% even with an ultrahigh current density of 30 A g⁻¹. The CV curves of the electrode are illustrated in Figure S18b (Supporting Information). It was determined that the *b* values

of the oxidation peaks were 1.00, 0.95, 1.01, and 0.73, respectively, and those of the reduction peaks were 1.04, 1.04, 1.04, and 0.90, respectively. Compared to the electrode with a thickness of ≈220 μm, thinner electrodes exhibited improved reaction kinetics at each charge/discharge state. This assertion was corroborated by the results of EIS. The phase angles of the electrode at charge/discharge stages *I*–*V* became more negative, measuring –85.4°, –72.5°, –61.1°, –72.1°, and –83.0° at 0.1 Hz, respectively, signifying stronger capacitance characteristics (Figure S18c,d, Supporting Information).

Owing to the expanded structure of the EG particles and porous nature of the EG electrode, thick electrodes with high active material loadings aimed at high-energy-density applications also demonstrated outstanding electrochemical performance. Figure S19 (Supporting Information) illustrates the GCD curves of electrodes with thicknesses of ≈430, 620, and 810 μm (corresponding to active material loadings of ≈30, 45, and 60 mg cm⁻², respectively). The electrodes maintained specific capacities of 88.8, 83.6, and 82.2 mAh g⁻¹ with a current density of 1 A g⁻¹, respectively. Meanwhile, electrode formulations can also be adjusted to further enhance the energy densities of corresponding devices. For instance, electrodes without conductive additive exhibited satisfactory electrochemical performance (Figure S20, Supporting Information).

In summary, the PTFE binder played a crucial role in achieving excellent electrochemical performance for the EG electrodes. First, its exceptional chemical resistance and high-temperature stability ensured the electrode's chemical and electrochemical stability. Second, its unique fibrillization binding mechanism ensured that the electrode could withstand severe volume expansion and form a porous structure, thereby providing superior cycling stability and rate capability. Finally, the use of PTFE greatly enhanced the flexibility in electrode formulation and preparation methods, allowing for the facile preparation of electrodes with varying compositions and thicknesses to meet a spectrum of application requirements.

2.4. Temperature Influences on Electrode Performance

The ANK-MSE system could maintain its molten state over a wide temperature range, which could potentially offer significant benefits in reducing the complexity and cost of battery thermal management systems. As a result, we tested the electrochemical performance of the EG electrode in the ANK-MSE system within the temperature range of 100–175 °C.

The ANK-MSE system exhibited high conductivities of 0.12, 0.15, 0.18, and 0.22 S cm⁻¹ at 100, 125, 150, and 175 °C, respectively (Figure S21, Supporting Information). Within this temperature range, increased temperature led to improvements in electrode specific capacities and half-cell energy efficiencies (Figure 4a,b). For example, with a current density of 5 A g⁻¹, the discharging capacities of the electrode at 100, 125, 150, and 175 °C reached 76.8, 84.3, 87.9, and 91.8 mAh g⁻¹, respectively, with corresponding half-cell energy efficiencies of 83.5%, 84.7%, 85.5%, and 86.5%, respectively (Figures S22 and S23, Supporting Information). It is worth noting that the electrolyte decomposition occurred at the end of charging with a current density of 1 A g⁻¹ at 175 °C, indicating the need to adjust the cutoff

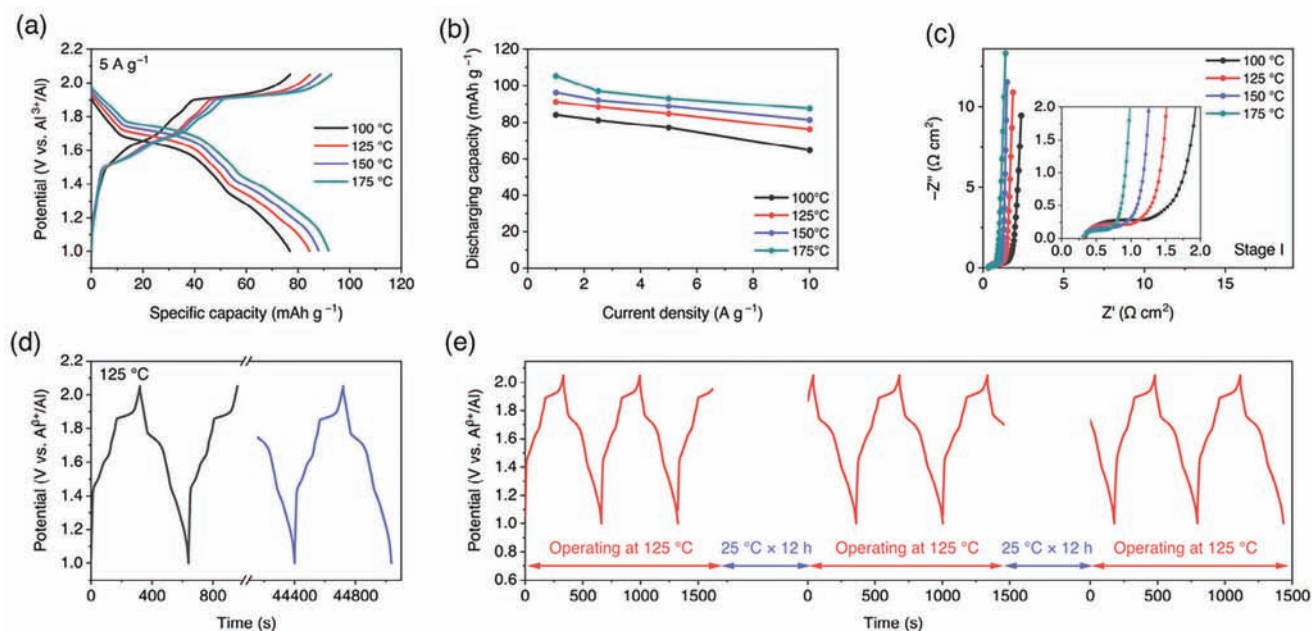


Figure 4. Temperature influences on electrode performance. a) GCD curves of the EG electrode with a current density of 5 A g^{-1} at different temperatures. b) Discharging capacities of the EG electrode with different current densities at different temperatures. c) Nyquist plots of the EG electrode at stage I at different temperatures. d) Self-discharge test of the EG electrode. The cell was fully charged and then kept at $125 \text{ }^\circ\text{C}$ for 12 h before operating again. The current density was 1 A g^{-1} . e) Freezing-thawing test. The cell was terminated and cooled down to $25 \text{ }^\circ\text{C}$ for 12 h during a charge and a discharge process, respectively. The current density was 1 A g^{-1} .

potential appropriately at higher temperatures (Figure S24, Supporting Information).

Observations from the CV curves obtained at various temperatures revealed that as temperature increased, the current densities corresponding to each peak increased. Moreover, the peak positions of each oxidation-reduction pair became closer, consistent with the results observed in the GCD tests (Figure S25, Supporting Information). Additionally, the fitting analysis revealed an increase in the b values for the O4 and R4 peaks, indicating an acceleration in the electrochemical activity of the electrode (Figure S26 and Table S2, Supporting Information). This observation was further substantiated by the EIS results. As seen in Figure S27 (Supporting Information), the phase angles within the low-frequency region of the electrode became more negative as the temperature increased. Moreover, the R_{ct} of the electrode significantly decreased with the temperature at all charged/discharged states, suggesting faster electron transport at elevated temperatures (Figure 4c; Figure S28, Supporting Information). For example, at stage I, the R_{ct} values at 100, 125, 150, and $175 \text{ }^\circ\text{C}$ were 0.71, 0.50, 0.38, and $0.24 \text{ } \Omega \text{ cm}^2$, respectively (Table S3, Supporting Information).

Due to the pseudocapacitive nature of the electrode's electrochemical reactions, the system was susceptible to self-discharge issues. After being fully charged and then kept at $125 \text{ }^\circ\text{C}$ for 12 h, the EG electrode experienced a gradual decrease in open-circuit potential (OCP) from 2.01 to 1.69 V (Figure S29, Supporting Information). Meanwhile, the stored energy was reduced to 71.6% of what would be expected in a normal discharge process (Figure 4d). Notably, below its eutectic point, the ANK-MSE would solidify and become ionically insulating, enabling us to leverage this phenomenon to suppress self-discharge. Figure 4e

illustrates that the cell was terminated and cooled down to $25 \text{ }^\circ\text{C}$ for 12 h during cycling. The OCP demonstrated negligible changes, and the cell operated steadily after being restarted.

2.5. 100-mAh-Scale Full-Cell Test

To validate the feasibility of large-scale application of the dry processing electrode, a full-cell with a capacity of $\approx 100 \text{ mAh}$ was fabricated (Figure 5a). The cell utilized aluminum foils as the anode and the EG electrodes as the cathode (Figure 5b). Each EG electrode was pressed into two Mo meshes, which served as the cathode current collector. Three pairs of anode and cathode sheets were inserted into the battery case made from PTFE, while glass fiber separators were employed between the electrodes to prevent short-circuits. After electrolyte filling and battery case sealing, the device was heated and operated.

The battery achieved capacities of 117.2, 115.4, and 100.7 mAh and energy efficiencies of 87.0%, 87.1%, and 78.7% with currents of 50, 100, and 500 mA (corresponding to current densities of 0.033, 0.66, and 0.33 A g^{-1}), respectively (Figure 5c). The battery exhibited greater voltage hysteresis compared to small-scale devices, possibly due to the larger voltage drop caused by the internal resistance of the electrode tabs and the high-temperature battery test system under higher currents. These factors are likely to be mitigated in large-scale production processes. The battery was further cycled for 100 cycles with a current of 500 mA, with a capacity retention of 99.6% and an average coulombic efficiency of 99.2% (Figure 5d). Meanwhile, the charge and discharge curves for the first and last cycles nearly overlapped, indicating excellent cycling stability (Figure 5e).

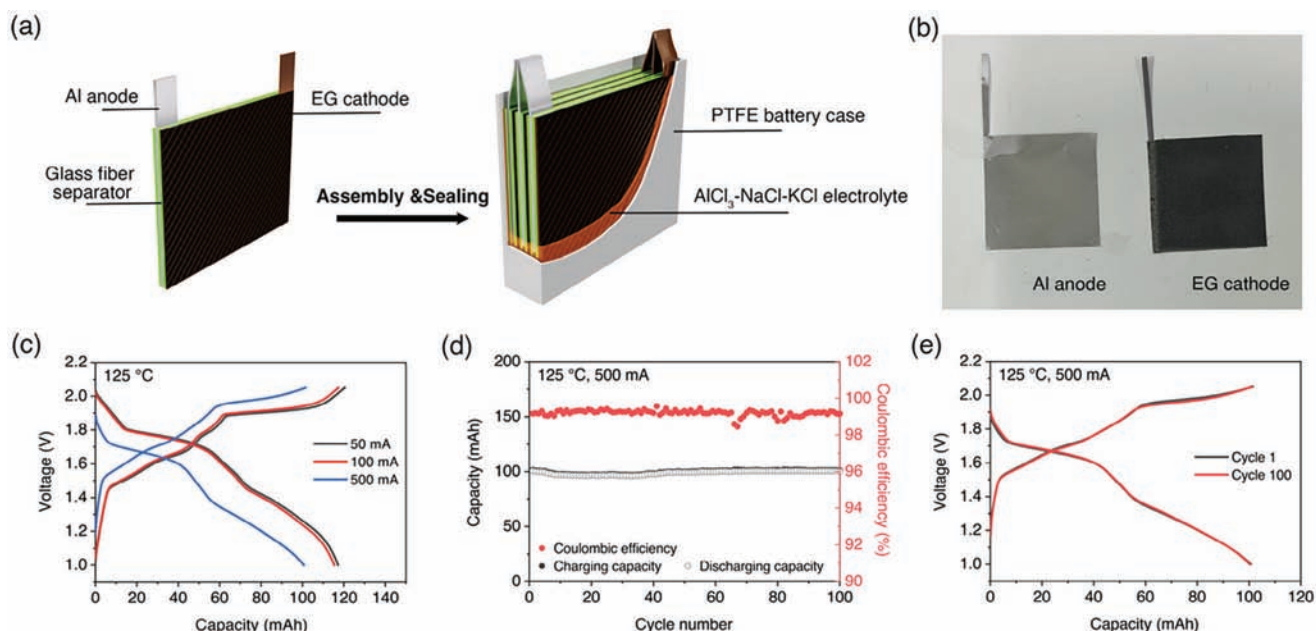


Figure 5. Electrochemical performance of the 100-mAh-scale Al-EG full-cell. a) Schematic diagram of the full-cell. b) Photograph of the Al anode and EG cathode. c) GCD curves with different currents at 125 °C. d, e) Cycling stability with a current of 500 mA at 125 °C.

The aforementioned findings underscore the promising potential of the Al-EG battery system for large-scale applications. Benefiting from the high ionic conductivity of the ANK-MSE and the porous architecture of the EG electrode, it exhibited commendable high rate performance while retaining a substantial active material loading. In comparison to other AIBs utilizing carbon-based cathodes, our EG electrode demonstrated markedly superior areal capacity, thus indicating enhanced practical viability (Figure S30, Supporting Information). Through techno-economic analysis, the Al-EG battery based on ANK-MSE yielded an energy density of 88.0 Wh kg⁻¹ and an energy cost of 18.4 \$ kW h⁻¹ based on the active materials (Table S4, Supporting Information). Our reported battery surpassed other MSB systems in terms of power density and lifetime (Figure S31, Supporting Information). Furthermore, owing to its lower operating temperature and absence of molten alkali metals, the Al-EG battery not only offered advantages in material and maintenance costs but also exhibited superior safety, which is a pivotal aspect for large-scale deployment.

3. Conclusion

In conclusion, our study presents an EG electrode for AIBs prepared via the dry electrode processing method with PTFE as the binder, which demonstrated superior electrochemical performance in the ANK-MSE system over a wide temperature range of 100 to 175 °C. The unique microstructure of the EG electrode, enabled by the PTFE fibrous network, accommodated the significant volume expansion associated with electrode intercalation reactions and ensured remarkable cycling stability over 10000 cycles. Moreover, a 100-mAh-scale Al-EG full-cell showcased its potential for large-scale applications. In addition, this work provides a universal and high-performance electrode preparation method

for MSBs. By demonstrating the applicability of PTFE binder in MSE environments, a variety of compound materials with high capacity, potential, and cycling stability, such as oxides and sulfides, which are extensively studied, can be applied in the future.

4. Experimental Section

Materials: EG, CB (Ketjenblack EC-600JD), and PTFE preparation (60 wt.% dispersion in H₂O) were purchased from Shenzhen Kejing Co., Ltd. Glass microfiber filters (Whatman 934-AH) were used as separators.

Electrode Preparation: EG, CB, and PTFE preparation were mixed with a small amount of ethanol added to aid PTFE dispersion. After the ethanol evaporated, the resultant mixture was then processed into a thin slice with a pressure of 10–50 MPa, and pressed into two molybdenum meshes. The EG electrode was dried in an oven at 60 °C overnight before use. The weight ratio of EG, CB, and PTFE was 0.80:0.10:0.10.

Electrolyte Preparation: The ANK-MSE was prepared in an argon-filled glove box (Etelux, Lab2000). AlCl₃, NaCl, and KCl powders were fully mixed with a molar ratio of 0.61:0.26:0.13. The mixture was heated in an alumina crucible to 125 °C for 12 h. The melts, which were clear and colorless, were poured out carefully and collected.

Device Assembly: For half-cells, the EG electrode was tested in a quartz container filled with the ANK-MSE, with aluminum foil as the reference electrode, and tantalum wire as the counter electrode. For full-cells, aluminum foils (200 μm, 5 cm × 5 cm) and EG electrode sheets (≈220 μm, 5 cm × 4.8 cm) were used as the anode and cathode, respectively. The EG electrode was pressed into two molybdenum meshes (200-mesh, 5 cm × 5 cm), which served as the cathode current collector. Three anode and cathode sheets were inserted into the battery case made from PTFE, while glass fiber separators (260 μm, 5.5 g m⁻², 5.5 cm × 5.5 cm) were employed between the electrodes to prevent short-circuits. After filling the case with the electrolyte (≈30 mL) and sealing it, the battery was heated and operated.

Materials Characterizations: The microstructures of the samples were characterized by SEM (Zeiss Merlin) and TEM (Joel JEM-2100F). The microstructure of the EG electrode was characterized by micro-CT (Zeiss

Xradia620 Versa). Phase identifications of the samples were analyzed by XRD (Rigaku D-Max-2500), XPS (Thermo Fisher ESCALAB 250 Xi XPS), and Raman spectroscopy (Horiba LabRAM HR Evolution, 532 nm laser). The surface areas, adsorption, and desorption isotherms, and pore size distributions of the samples were analyzed by BET tests (Micromeritics ASAP 2460). The eutectic point of the electrolyte was analyzed by differential scanning calorimetry (DSC) (TA-DSC25).

Electrochemical Characterization: GCD and CV tests of the EG electrodes and the Al-EG batteries were conducted on an electrochemical workstation (CHI 660e). Electrolyte conductivities, EIS plots, and self-discharge profiles were measured with an electrochemical workstation (Metrohm Autolab). Cycling performance was tested using a battery test system (LAND 2001CT).

Supporting Information

Supporting Information is available from the Wiley Online Library or from the author.

Acknowledgements

This work was supported by the Basic Science Center Program of the National Natural Science Foundation of China (NSFC) Grant No. 52388201, NSFC Grants No. 52325312, and Beijing Municipal Science & Technology Commission, Administrative Commission of Zhongguancun Science Park No. Z231100006023020.

Conflict of Interest

The authors declare no conflict of interest.

Author Contributions

K.W. and Y.W. contributed equally to this work. K.W. and Y.W. performed conceptualization, methodology, investigation, wrote the original draft. C.Y. and M.Y. performed methodology, investigation, wrote, reviewed, and edited the draft. C.L., Y.Z., and T.D. performed investigation, wrote, reviewed, and edited the draft. Y.L. performed methodology, wrote, reviewed, and edited the draft. K.L. performed methodology, supervision, wrote, reviewed, and edited the draft. M.L. performed wrote, reviewed, and edited the draft. H.W. performed conceptualization, methodology, supervision, wrote, reviewed, and edited the draft.

Data Availability Statement

The data that support the findings of this study are available from the corresponding author upon reasonable request.

Keywords

aluminum-ion battery, dry electrode processing, molten salt

Received: February 4, 2024

Revised: April 1, 2024

Published online:

[1] A. A. Kebede, T. Kalogiannis, J. Van Mierlo, M. Bercibar, *Renewable Sustainable Energy Rev.* **2022**, *159*, 112213.

- [2] S. Koohi-Fayegh, M. A. Rosen, *J. Energy Storage* **2020**, *27*, 101047.
 [3] Z. Zhu, T. Jiang, M. Ali, Y. Meng, Y. Jin, Y. Cui, W. Chen, *Chem. Rev.* **2022**, *122*, 16610.
 [4] Y. Gao, Z. Pan, J. Sun, Z. Liu, J. Wang, *Nano-Micro Lett.* **2022**, *14*, 94.
 [5] F. Wu, J. Maier, Y. Yu, *Chem. Soc. Rev.* **2020**, *49*, 1569.
 [6] H. Liu, X. Zhang, S. He, D. He, Y. Shang, H. Yu, *Mater. Today* **2022**, *60*, 128.
 [7] K. Wang, Z. Chen, K. Liu, C. Yang, H. Zhang, Y. Wu, Y. Long, H. Liu, Y. Jin, M. Li, H. Wu, *Energy Environ. Sci.* **2022**, *15*, 5229.
 [8] P. Masset, R. A. Guidotti, *J. Power Sources* **2007**, *164*, 397.
 [9] M. M. Li, J. M. Weller, D. M. Reed, V. L. Sprenkle, G. Li, *Joule* **2023**, *7*, 619.
 [10] H. Li, H. Yin, K. Wang, S. Cheng, K. Jiang, D. R. Sadoway, *Adv. Energy Mater.* **2016**, *6*, 1600483.
 [11] S. Licht, B. Cui, J. Stuart, B. Wang, J. Lau, *Energy Environ. Sci.* **2013**, *6*, 3646.
 [12] V. Giordani, D. Tozier, J. Uddin, H. Tan, B. M. Gallant, B. D. McCloskey, J. R. Greer, G. V. Chase, D. Addison, *Nat. Chem.* **2019**, *11*, 1133.
 [13] Y. G. Zhu, G. Leverick, A. Accogli, K. Gordiz, Y. Zhang, Y. Shao-Horn, *Energy Environ. Sci.* **2022**, *15*, 4636.
 [14] P. Meng, Z. Yang, J. Zhang, M. Jiang, Y. Wang, X. Zhang, J. Luo, C. Fu, *Energy Storage Mater.* **2023**, *63*, 102953.
 [15] Y. Song, S. Jiao, J. Tu, J. Wang, Y. Liu, H. Jiao, X. Mao, Z. Guo, D. J. Fray, *J. Mater. Chem. A* **2017**, *5*, 1282.
 [16] J. Wang, X. Zhang, W. Chu, S. Liu, H. Yu, *Chem. Commun.* **2019**, *55*, 2138.
 [17] J. Tu, J. Wang, H. Zhu, S. Jiao, *J. Alloys Compd.* **2020**, *821*, 153285.
 [18] B. Cui, S. Licht, *J. Mater. Chem. A* **2014**, *2*, 10577.
 [19] D. J. Bradwell, H. Kim, A. H. C. Sirk, D. R. Sadoway, *J. Am. Chem. Soc.* **2012**, *134*, 1895.
 [20] K. Wang, K. Jiang, B. Chung, T. Ouchi, P. J. Burke, D. A. Boysen, D. J. Bradwell, H. Kim, U. Muecke, D. R. Sadoway, *Nature* **2014**, *514*, 348.
 [21] R. A. Guidotti, P. Masset, *J. Power Sources* **2006**, *161*, 1443.
 [22] J. Ko, S. H. Kang, H. W. Cheong, Y. S. Yoon, *J. Korean Ceram. Soc.* **2019**, *56*, 233.
 [23] W. Yang, L. Zhou, Z. Luo, J. Zhu, W. Yang, D. Li, L. Fu, *Adv. Eng. Mater.* **2020**, *22*, 2000299.
 [24] J. Li, J. Fleetwood, W. B. Hawley, W. Kays, *Chem. Rev.* **2022**, *122*, 903.
 [25] H. J. Chang, X. Lu, J. F. Bonnett, N. L. Canfield, S. Son, Y. C. Park, K. Jung, V. L. Sprenkle, G. Li, *J. Power Sources* **2017**, *348*, 150.
 [26] N. A. Salleh, S. Kheawhom, N. Ashrina A Hamid, W. Rahiman, A. A. Mohamad, *J. Mater. Res. Technol.* **2023**, *23*, 3470.
 [27] F. Zou, A. Manthiram, *Adv. Energy Mater.* **2020**, *10*, 2002508.
 [28] Y. Ma, J. Ma, G. Cui, *Energy Storage Mater.* **2019**, *20*, 146.
 [29] F. Hippauf, B. Schumm, S. Doerfler, H. Althues, S. Fujiki, T. Shiratsushi, T. Tsujimura, Y. Aihara, S. Kaskel, *Energy Storage Mater.* **2019**, *21*, 390.
 [30] Z. Zhang, L. Wu, D. Zhou, W. Weng, X. Yao, *Nano Lett.* **2021**, *21*, 5233.
 [31] T. Jiang, P. He, G. Wang, Y. Shen, C.-W. Nan, L.-Z. Fan, *Adv. Energy Mater.* **2020**, *10*, 1903376.
 [32] Y. Lu, C. Z. Zhao, H. Yuan, J. K. Hu, J. Q. Huang, Q. Zhang, *Matter* **2022**, *5*, 876.
 [33] Y. Zhang, F. Huld, S. Lu, C. Jektvik, F. Lou, Z. Yu, *Batteries* **2022**, *8*, 1.
 [34] N. Verdier, G. Foran, D. Lepage, A. Pr  b  , D. Aym  -Perrot, M. Doll  , *Polymers* **2021**, *13*, 323.
 [35] S. W. Pr  mper, W. Frank, *Acta Crystallogr. Sect. E Crystallogr. Commun.* **2017**, *73*, 1426.
 [36] Y. Jiang, J. Liu, *Energy Environ. Mater.* **2019**, *2*, 30.
 [37] X. Dong, H. Xu, H. Chen, L. Wang, J. Wang, W. Fang, C. Chen, M. Salman, Z. Xu, C. Gao, *Carbon* **2019**, *148*, 134.

- [38] X. Xu, K. S. Hui, K. N. Hui, J. Shen, G. Zhou, J. Liu, Y. Sun, *Chem. Eng. J.* **2021**, *418*, 129385.
- [39] M. Lin, M. Gong, B. Lu, Y. Wu, D. Wang, M. Guan, M. Angell, C. Chen, J. Yang, B. Hwang, H. Dai, *Nature* **2015**, *520*, 324.
- [40] K. V. Kravchyk, S. Wang, L. Piveteau, M. V. Kovalenko, *Chem. Mater.* **2017**, *29*, 4484.
- [41] S. C. Jung, Y. J. Kang, D. J. Yoo, J. W. Choi, Y. K. Han, *J. Phys. Chem. C* **2016**, *120*, 13384.
- [42] G. Wang, M. Yu, J. Wang, D. Li, D. Tan, M. Löffler, X. Zhuang, K. Müllen, X. Feng, *Adv. Mater.* **2018**, *30*, 1800533.
- [43] J. S. Ko, C. H. Lai, J. W. Long, D. R. Rolison, B. Dunn, J. N. Weker, *ACS Appl. Mater. Interfaces* **2020**, *12*, 14071.